PAPER

Check for updates

Red emission of copper aluminate synthesized *via* chemical and bio-mediated routes

N. R. Srinath,[a] H. C. Manjunatha, [ID] *[a] Y. S. Vidya, [ID] *[b] R. Munirathnam,[a] K. N. Sridhar,[c] S. Manjunatha[d] and E. Krishnakanth[a]

For the first time, copper aluminate nanoparticles (NPs) are synthesized by a combustion method using urea as a fuel (CAOU) and *Ocimum sanctum* (tulsi) extract as a reducing agent (CAOT). The Bragg reflections of the as-formed product confirm the formation of a cubic phase with $Fd\bar{3}m$ space group. The crystallite size, crystallinity and other structural parameters are discussed. The surface morphology of CAOU is agglomerated in nature whereas that of CAOT is hexagonal in shape. The smaller crystallite size CAOT NPs show a higher energy band gap. The photoluminescence (PL) analysis excited at 302 nm shows that the CIE coordinates fall in the red region. The oxygen defects are mainly responsible for the PL emission. The CCT coordinates confirm that both CAOU and CAOT NPs can find an application in warm light emitting diodes.

I. Introduction

Due to their excellent combination of key characteristics including high melting point, hardness, relatively low density, high mechanical strength, high resistance to chemical attack, wide energy band gap, and high electrical resistivity, aluminates have recently attracted significant attention from academia and the industrial sector.[1] These properties make them useful in sensors,[2] biomedical devices,[3] displays[4] *etc.* Numerous studies have been employed on different aluminates such as $ZnAl_2O_4$,[5] $CuAl_2O_4$,[6] $CaAl_2O_4$ (ref. 7) *etc.*

Among the aluminate spinels, the nanocrystalline copper aluminate ($CuAl_2O_4$) is known to be active in the degradation of some organic compounds[8] and in the reduction of nitrogen monoxide with carbon monoxide.[9] Similar to other aluminates, copper aluminate finds an application as a sensor material and as a ceramic pigment in ceramic coatings.[10] In a cubic stoichiometry, Cu^{2+} ions occupy tetrahedral positions whereas Al^{3+} ions occupy octahedral positions. In addition to this, Al^{3+} ions are distributed equally between both the coordinates.[11] In the copper aluminate Cu–Al–O system, chemical and structural relations are more complex. In the atmosphere, two copper oxides can form: CuO and Cu_2O. Moreover, this system provides two stable copper aluminates. One with spinel structure ($CuAl_2O_4$) and other with delafossite structure ($CuAlO_2$). Among these two, copper

aluminate with cubic spinel crystal structure possesses high thermal stability and high mechanical resistance. Substitution of metal ions in tetrahedral or octahedral sites improves the optical, magnetic and catalytic properties of the nanomaterial.

In the last few decades, nanomaterials (NMs) have become a crucial component of advanced display technology.[12] Materials that produce light are sensitive to light exposure. They emit light after absorbing light at a specific wavelength, usually UV light and emit the light at another wavelength in the visible region.[13] A number of research works have been carried out on the PL property of aluminates. Gadolinium aluminate as a host gives green emission. This green emission can be enhanced after doping with terbium ions.[14] Barium magnesium aluminate is a blue phosphor; after thermal degradation it gives green emission.[15] Pure blue emission is observed for magnesium strontium aluminate.[16] Even though a number of research works have been carried out on pure/doped aluminates, there is a little data on the optical properties of copper aluminate.[17,18]

For all these applications, synthesis of copper aluminate with high purity, small crystallite size and high surface area is required. This can be achieved through a suitable synthesis route. Copper aluminate has been synthesized using different routes such as sonochemical,[19,20] sol gel,[21,22] soft chemical route,[10] *etc.* Among all these routes, combustion synthesis is a more convenient method for the synthesis of nanomaterials. Through this method, one can synthesise single phase NMs with homogeneous structure at low temperatures. In this method, generally, chemical fuels are used to get the single phase. Because of these outstanding properties, a combustion method has been chosen to synthesize the NPs. However, nowadays, the use of plant extracts as a reducing agent or capping agent to tune the properties of NMs has become a prominent area of research work in materials science. In this

[a]Department of Physics, Government College for Women, Kolar-563101, Karnataka, India. E-mail: manjunathhc@rediffmail.com

[b]Department of Physics, Lal Bahadur Shastri Government First Grade College, RT Nagar, Bangalore-560032, Karnataka, India. E-mail: vidyays.phy@gmail.com

[c]Department of Physics, Government First Grade College, Kolar-563101, Karnataka, India

[d]Department of Chemistry, B.M.S College of Engineering, Bengaluru-560019, Karnataka, India
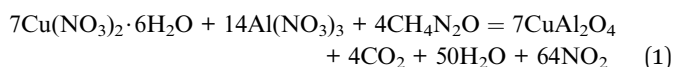
context, *Ocimum sanctum* (tulsi) extract is used as a reducing agent and compared with the same NMs synthesized using urea as a fuel. The effect of chemical fuel and tulsi extract as a reducing agent on the optical properties of copper aluminate are explored.

The plant *Ocimum sanctum* is a "Mother medicine of Nature" as well as "Queen of Herbs". It has antioxidant and antidiarrhoeal properties. Eugenol is the primary active ingredient in tulsi. Chemicals including caryophyllene, terpinene-4-ol, eugenol methyl ester, 3-carene, vitamin C, gallic acid, vanillin, carvacrol, palmitic acid and vitamin A are other chemicals extracted from tulsi. Hence in the present study, copper aluminate is synthesized by using a chemical and tulsi extract as a reducing agent *viz.* CAOU and CAOT, for the purposes of comparison of the resulting structural and optical properties. The photoluminescence behavior was studied for applications in energy efficient display technology.

II. Materials and methods

A. Synthesis of $CuAl_2O_4$ using urea as a fuel (CAOU)

Initially, 5 g of $Cu(NO_3)_2 \cdot 6H_2O$, 0.58 g of urea as a fuel and 7.2 g of $Al(NO_3)_3$ were dissolved in a minimum amount of nitric acid under magnetic stirring at room temperature for 3 h. The oxidizer-to-fuel ratio is maintained as one. The above solution is placed in a preheated muffle furnace. Within a short interval of time, the mixture catches fire and undergoes an exothermic reaction, which results in the formation of the product. The as-formed product (2.98 g yield) is collected without any further calcination followed by grinding.

$$7Cu(NO_3)_2 \cdot 6H_2O + 14Al(NO_3)_3 + 4CH_4N_2O = 7CuAl_2O_4 \\ + 4CO_2 + 50H_2O + 64NO_2 \quad (1)$$

B. Synthesis of $CuAl_2O_4$ using tulsi extract as a reducing agent (CAOT)

Initially, 5 g of $Cu(NO_3)_2 \cdot 6H_2O$ and 7.2 g of $Al(NO_3)_3 \cdot 9H_2O$ is dissolved in minimum amount of nitric acid. Then 15 ml of *Ocimum sanctum* (tulsi) extract was subsequently added as a reducing agent to the above solution under magnetic stirring at room temperature for 3 h. The above solution is placed in a pre-heated muffle furnace. Within a short interval of time, the mixture catches the fire, undergoing exothermic reaction, which results in the formation of the product. The as-formed product with 3.12 g of yield is collected without any further calcination followed by grinding. The flowchart for the synthesis of $CuAl_2O_4$ using tulsi extract as a reducing agent and urea as a fuel is shown in Fig. 1.

$$7Cu(NO_3)_2 \cdot 6H_2O + 14Al(NO_3)_3 + 15 \text{ ml tulsi extract} \\ = 7CuAl_2O_4 + 4CO_2 + 50H_2O + 64NO_2 \quad (2)$$
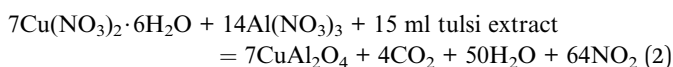
C. Characterization

Powder X-ray diffraction (PXRD) analysis is carried out utilizing a PAN analytical X'Pert-PRO MPD with Cu Kα radiation.
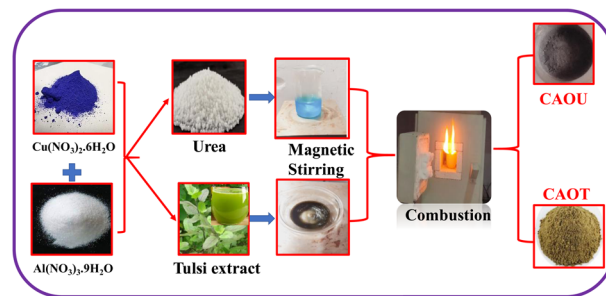

Fig. 1 Flowchart for the synthesis of CAOU and CAOT NPs.

Scanning Electron Microscopy (SEM) analysis is carried out using a SEM, Hitachi, and S-4200. To record UV absorption spectra, a V-730 double-beam UV-Visible spectrometer is used. A PerkinElmer L1280134 is used to record Fourier Transform Infrared Spectroscopy. The photoluminescence excitation and emission spectra were recorded on a Horiba Fluorolog Spectrofluorometer at room temperature.

III. Results and discussion

A. PXRD analysis of CAOU and CAOT NPs

The crystalline structure and purity of the sample can be obtained by PXRD analysis. Fig. 2 shows the PXRD pattern of as-formed CAOU and CAOT NPs. The Bragg reflections at 32.44, 35.58, 38.72, 48.77, 53.72, 58.08, and 61.68° 2θ values correspond to (111), (220), (311), (331), (422), (400) and (511) respectively. These diffraction peaks can be indexed to the pure cubic phase with $Fd\bar{3}m$ space group (JCPDS no. 78-0556). No other impurity related peaks are detected. The PXRD intensity of CAOT was found to be higher compared to CAOU. The reducing agent/fuel plays an important role in the stoichiometry, intensity, defect centers and size of the NPs.[23] The crystallite size was estimated by using Scherrer's and W–H plot methods.[24] The crystallite size of CAOU and that of CAOT was found to be 25 and 20 nm respectively. The green extract helps to tune the crystallite size of the NPs. The crystallinity of the sample was found to be improved in CAOT. The other structural parameters such as strain, dislocation density, and structural
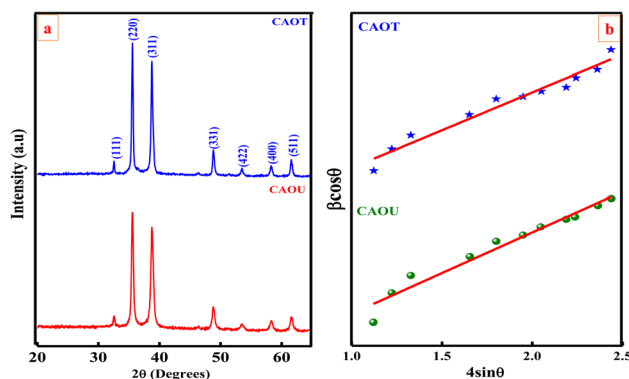

Fig. 2 (a) PXRD analysis and (b) W–H plot of CAOT and CAOU NPs.

Table 1 Crystallite size (Scherrer's and W–H plot method), crystallinity and other structural parameters of the CAOU and CAOT NPs

Type	Crystal size (nm)		Crystallinity (%)	Strain, $\times 10^{-3}$	Dislocation density, $\times 10^{15}$ lines per m^2	SF
	Scherrer	W–H				
Tulsi	20.16	19.05	93.9	2.1	2.75	0.35
Urea	24.37	23.87	94.03	2.03	0.51	0.35

factor are determined and tabulated in Table 1. Similar to chemical fuel, the green extract which is ecofriendly helped in retaining the single cubic phase.

B. Rietveld analysis of copper aluminate NPs

Rietveld refinement analysis was performed by using the FULLPROOF suite program to get precise information about the crystal structure and lattice parameters. The refined parameters are summarized in Table 2. Good agreement is obtained between the experimental relative intensity and stimulated intensity Fig. 3. The goodness of fit (GOF) is used to estimate the quality of the refined data. In the present study, GOF was found to be 0.96, which confirms that the experimental and theoretical plots fit together well. Diamond software was used to create the packing diagram using the Rietveld refinement parameters (inset of Fig. 3).

C. Surface morphology analysis of CAOU and CAOT NPs

The surface morphology images taken at different magnifications for CAOU and CAOT NPs are displayed in Fig. 4a–d respectively. The CAOU NPs are agglomerated in nature, such that no regularity is observed in the shape of the NPs. Particle
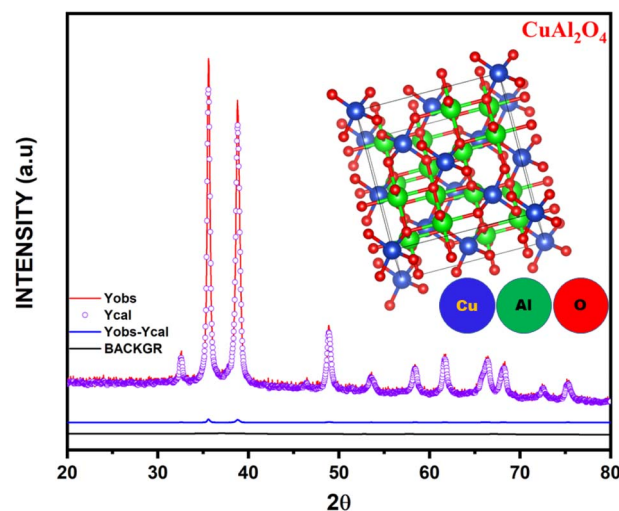

Fig. 3 Rietveld refinement (inset: packing diagram) of $CuAl_2O_4$ NPs. (Yobs - Observed Intensity, Ycal - Intensity obtained from the experiment, BACKGR- Background)

Table 2 Rietveld parameters of copper aluminate NPs

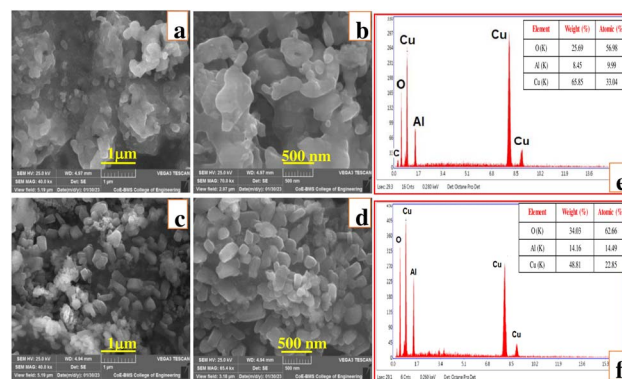| Parameters	
Crystal system	Cubic
Space group	$Fd\bar{3}m$
Space group number	227
Lattice parameters	
a (Å)	8.075
b (Å)	8.075
c (Å)	8.075
Unit cell volume (Å)^3	526.535
Atomic co-ordinates	
$x = y = z$	
Cu	0
Al	0.625
O	0.375
R-Factors	
R_p	8.01
R_{wp}	10.5
R_{exp}	7.11
X^2	2.18
R_{Bragg}	5.78
R_f	3.1

Fig. 4 (a–d) SEM images at different magnifications, (e and f) EDAX spectrum, (inset: elemental composition) of CAOU (top row) and CAOT (bottom row) NPs.

aggregation arises due to the reduction in surface free energy of the particles by increasing their size and decreasing their surface area. The adherence of particles to one another by weak forces causes the aggregation of nanoparticles, resulting in submicron/micron sized entities.[25] The agglomeration of NPs is the characteristic of the materials synthesized *via* combustion method. No such agglomeration is observed in CAOT NPs. The surface morphology consists hexagonal shaped NPs which are arranged one above the other. No voids or pores are observed.

The Energy Dispersive Analysis X-ray (EDAX) spectra confirms the presence of only Cu, Al and O elements in CAOU and CAOT (Fig. 4e and f, respectively). The insets of Fig. 4e and f depict the atomic and weight percentages of these elements present in the synthesized samples. Weight and atomic percentage of oxygen was found to be more in CAOT than that of CAOU. Thus, green extracts supports and enriches the oxygen content in the synthesized sample.

D. TEM morphological analysis of CAOU and CAOT NPs

Fig. 5a shows the TEM image of CAOU NPs. The image clearly indicates the formation of agglomerated NPs. Fig. 5b and c depict the HRTEM images of the NPs. The lattice fringes are clearly visible (Fig. 5c). For those lattice fringes, the interplanar spacing of 0.2854, 0.1554 and 0.2434 nm correspond to the (220), (511) and (311) planes in the cubic structure of the copper aluminate. The crystallite size determined from the TEM image is found to be 25 nm which is in accordance with the size estimated by Scherrer's method. No other interplanar spacings corresponding to the CuO or Al_2O_3 crystalline phases are observed. The SAED pattern is depicted in Fig. 5d. The SAED pattern's observed diffraction rings amply demonstrate good crystallinity. These diffraction rings were assigned to the cubic phase of copper aluminate and were indexed to the (311), (331), (220), and (511) planes. These findings support the XRD analysis and confirms the formation of pure copper aluminate. Similar observations were also made in the TEM images and SAED pattern of CAOT NPs (Fig. 6a–d). But compared to CAOU, less good crystallinity is observed in CAOT NPs.

E. FTIR spectroscopic analysis of CAOU and CAOT NPs

The FTIR spectra were recorded from 4000–400 cm^{-1} to show the different functional groups present in the as-formed CAOU
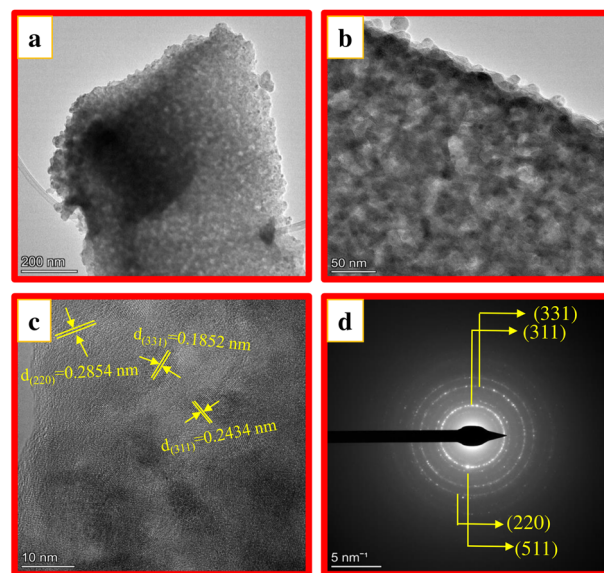

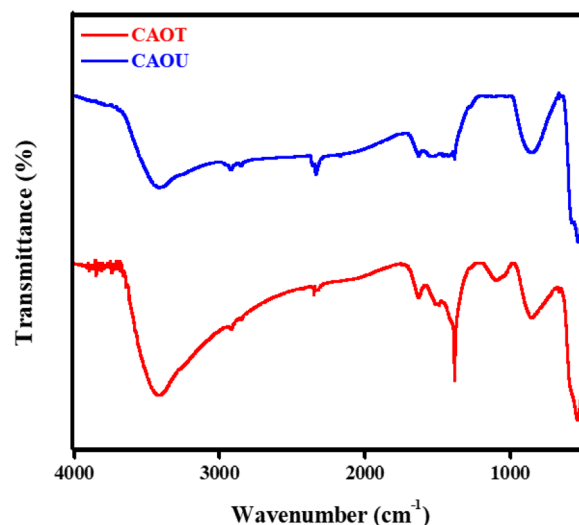Fig. 6 (a) TEM image (b and c) HRTEM image and (d) SAED pattern of CAOT NPs.

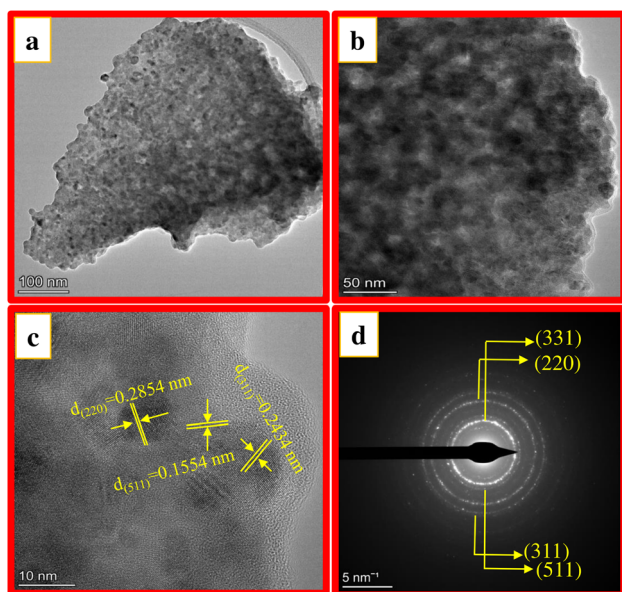Fig. 7 FTIR spectroscopic analysis of the CAOU and CAOT NPs.

and CAOT NPs (Fig. 7). The different functional groups and their corresponding wavenumbers are tabulated in Table 3. As we observed from Fig. 7, compared to CAOU, more IR absorption peaks are observed in CAOT between 1000 and 1550 cm^{-1}. The IR absorption peak observed at 1064 and 1100 cm^{-1} corresponds to an asymmetric vibration of C–O and C–O–C related to the beta glycosidic linkage in the cellulose of the tulsi extract.[30] A sharp peak with a center at 1391 cm^{-1} can indicate the presence of carboxylic components.

F. UV-visible analysis of CAOU and CAOT NPs

The percentage of incident radiation that a material absorbs over a range of electromagnetic radiation frequencies can be obtained from the absorption spectrum. The UV-Visible

Fig. 5 (a) TEM image (b and c) HRTEM image and (d) SAED pattern of CAOU NPs.

Table 3 FTIR analysis, functional group, wavenumber and their respective remarks of CAOU and CAOT NPs

Functional groups and their remarks	Wavenumber (cm^{-1})		References
	CAOU	CAOT	
–OH stretching of absorbed water	3405	3441	26
H–O–H bonding of absorbed water	1620	1644	26
Lattice vibrations of tetra and octahedrally coordinated metal ions	537	532	27
Al^{3+} occupied the tetrahedral site	853	853	28
C–O vibrations		1090	29
C=C vibrations		1405	29

absorption spectra recorded from 200–800 nm show a broad absorption spectra in the case of both CAOU and CAOT (Fig. 8a). Light scattering, from particles suspended in the sample comparable in size to the incident wavelength (250–300 nm) can reduce the amount of light reaching the detector leading to an increase in apparent absorbance. UV-Visible spectroscopy information may be presented as a graph of absorbance, optical density (OD) or transmittance as a function of wavelength. OD and absorbance both measure the amount of light intensity lost in an optical component, but OD takes into consideration loss from light scattering whereas absorbance does not. If very little light scattering is present in a measurement, then OD may be approximated directly using absorbance and Beer–Lambert's law may be used. Even though scattering is associated with the interaction of UV Visible light with the nanoparticles, light scattering does not affect the molar extinction coefficient of a compound. Furthermore, the measured spectrum in UV-Visible spectroscopy corresponds to the absorbance and hence, the impact of light scattering on UV-Visible measurements is negligible. The broadness of the spectra ranges from 255 to 395 nm followed by a long tail in the visible region. At each energy level, a number of vibrational energies are available. The transitions between the different vibrational energy levels are mainly responsible for the peak broadening. Based on this UV-Visible absorption spectra, the direct energy band gap was determined using Wood and Tauc's relation. The tangent extrapolation to the X-axis obtained from the plot of $(\alpha h\nu)^2$ vs. $h\nu$ gives the energy gap of the synthesized nanomaterial (Fig. 8b). The calculated direct energy band gap was found to be 3.05 and 2.82 eV for CAOT and CAOU respectively. The decrease in crystallite size of CAOT can be correlated to the increase in energy band gap. Grain size affects the energy gap as a consequence of the charge carrier movement confinement in a limited space. As the size decreases the energy gap increases. As the crystallite size decreases, electron hole pairs are much closer together and the coulombic interaction between them increases giving an overall higher kinetic energy. This increase in kinetic energy leads to the expansion of the band gap.
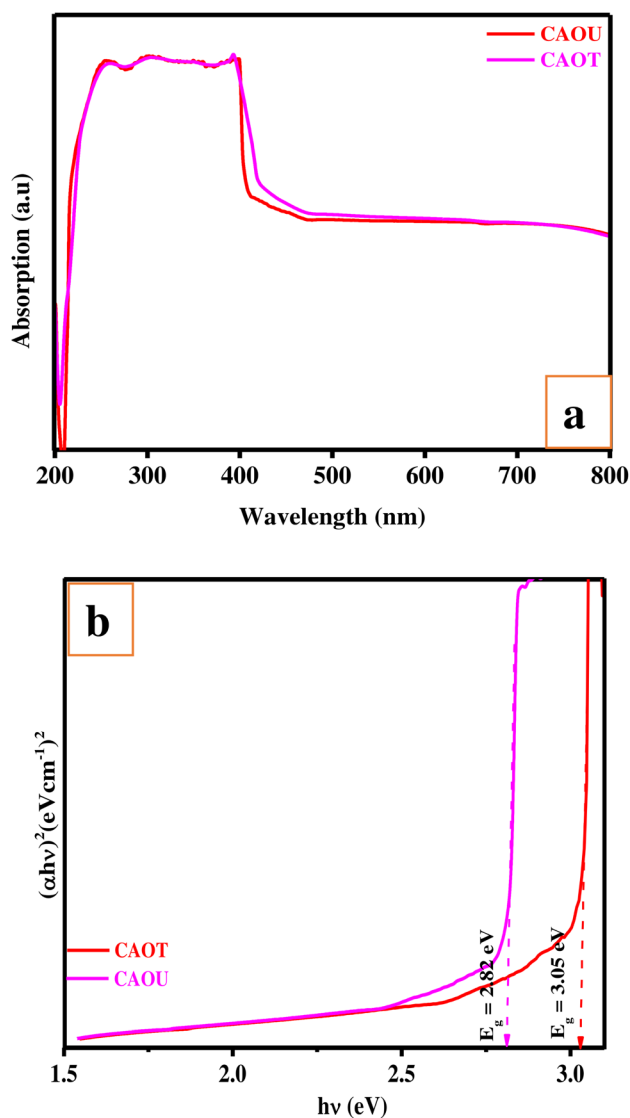
G. Photoluminescence analysis of CAOU and CAOT NPs

PL measurements are carried out on CAOU and CAOT NPs to understand the recombination phenomenon in the host matrix. The PL excitation spectrum was recorded by monitoring the emission wavelength at 610 nm (Fig. 9a). The excitation spectrum of CAOT NPs contains a sharp intense peak at 302 nm which can be attributed to transitions involved in the copper aluminate.[17] The excitation spectrum taken for CAOU NPs is similar except the small variation in intensity. By choosing the 302 nm as an excitation wavelength, an emission spectrum was
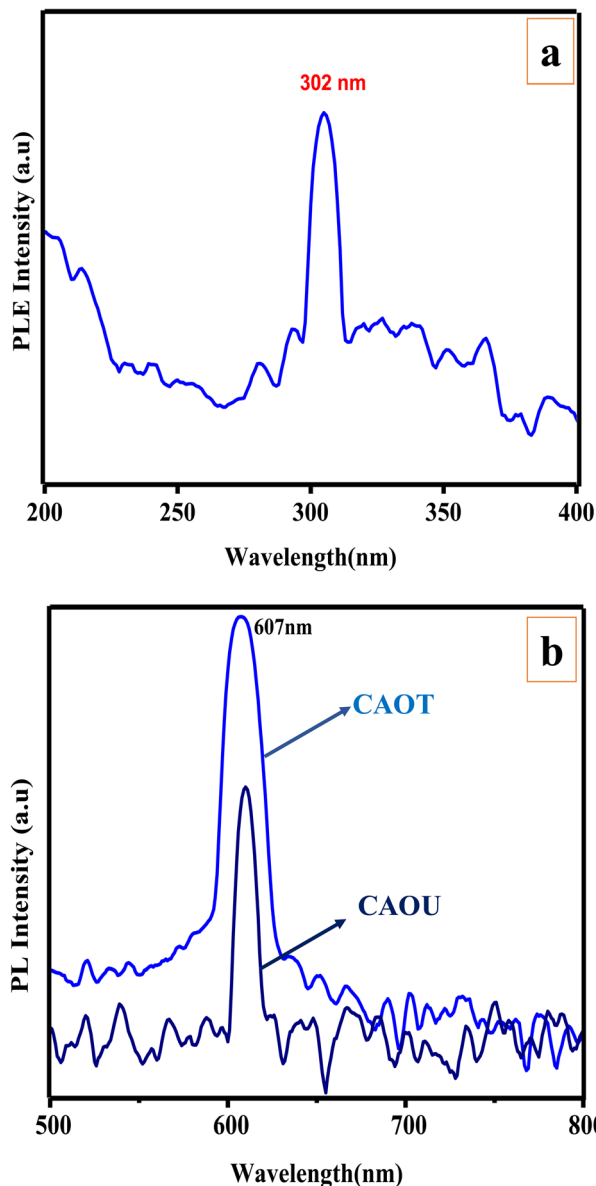

Fig. 8 (a) UV-Visible absorption spectra of CAOU and CAOT NPs. (b) Wood and Tauc's plot of CAOU and CAOT NPs.

Fig. 9 (a) PL excitation spectrum. (b) PL emission spectra (λ_{ex} = 350 nm) of the as-formed and calcined CAOT and CAOU NPs.
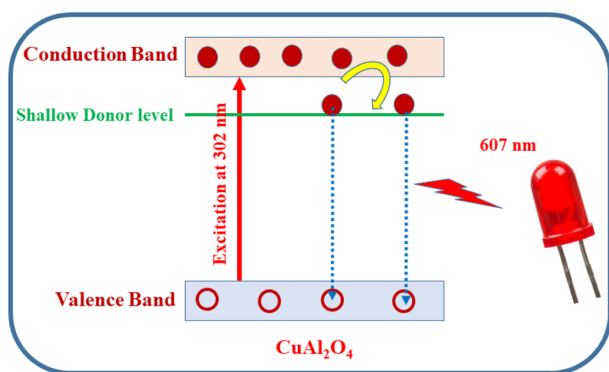

Fig. 10 Pictorial representation of the PL excitation and red emission of $CuAl_2O_4$ NPs.
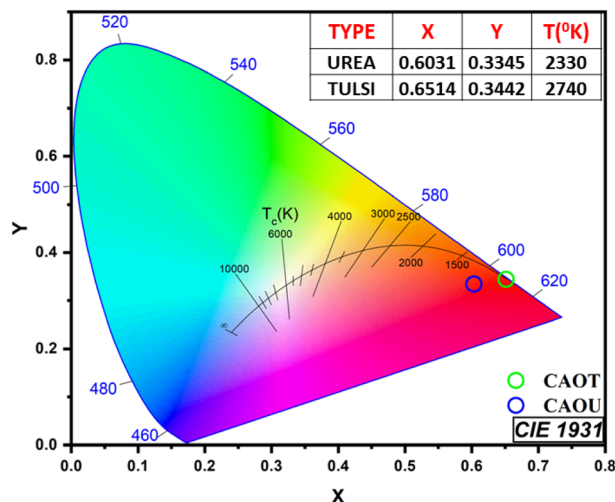

Fig. 11 CIE spectra of the as-formed and calcined CAOT and CAOU NPs.

recorded for CAOU NPs. The emission spectrum contains a sharp intense peak at 607 nm (Fig. 9b). No other additional peaks are observed. The emission spectrum is associated with the interstitial oxygen species. The electron transition takes place from shallow donor levels to the valence band. The defects provide the donor levels near the conduction band edge of $CuAl_2O_4$. Due to the lengthy lifetime of these levels, electrons in the conduction band (CB) initially stay back at the shallow donor level before recombining with the holes in the valence band.[31] A similar emission spectra was obtained for CAOT also except the variation in intensity. The highest intensity of CAOT indicates the higher rate of recombination of electrons and the holes. The pictorial representation for the PL excitation and emission is shown in Fig. 10.

Using the PL emission spectra, the chromaticity coordinates of CAOU and CAOT nanophosphors for luminous color are obtained from the Commission Internationale De L'Éclairage (CIE) 1931 colour space. The CIE coordinates (0.6514, 0.3443) and (0.6031, 0.3345) for CAOT and CAOU respectively fall in the red region (Fig. 11). The intensity of the redness is found to be greater for CAOT than CAOU. From the CIE coordinates, color correlated temperature was calculated to understand the technical applicability of the sample. The CCT value for both CAOT and CAOU was found to be less than 5000 K which is regarded as 'warm light emission' and meets the need of illuminating devices.

IV. Summary

In the present work, for the first time, copper aluminate was successfully synthesized by using two different fuels/reducing agents. The effect of urea as a chemical fuel and tulsi extract as a green reducing agent on the structural, optical are discussed. The diffraction patterns confirm the cubic phase in both the samples, but the crystallite size was found to be smaller and the direct energy band gap was found to be higher

for CAOT NPs. Green reducing agent helps in tuning the energy band gap of the synthesized NPs. The oxygen defects form a shallow donor level below the conduction band. The electrons present in the conduction band stay back in the shallow donor level and thereafter undergo recombination with holes present in the valence band. PL analysis, CIE and CCT coordinates confirm that the present synthesized CAOU and CAOT NPs could find an application in warm red light emitting diodes. But the intensity of red emission was found to be higher for CAOT than CAOU NPs.

Conflicts of interest

There is no conflicts to declare.

References

1 I. Ganesh, A review on magnesium aluminate ($MgAl_2O_4$) spinel: synthesis, processing and applications, *Int. Mater. Rev.*, 2013, **58**, 63.

2 C. Doroftei and L. Leontie, Porous nanostructured gadolinium aluminate for high-sensitivity humidity sensors, *Materials*, 2021, **14**, 7102.

3 T. Andrade, G. Santos, I. Oliveira and V. Pandolfelli, Synthesis optimization of calcium aluminate cement phases for biomedical applications, *Mater. Res.*, 2015, **18**, 382.

4 P. Jisha, S. Prashantha and H. Nagabhushana, Luminescent properties of Tb doped gadolinium aluminate nanophosphors for display and forensic applications, *J. Sci.: Adv. Mater. Devices*, 2017, **2**, 437.

5 M. K. Habibi, S. M. Rafiaei, A. Alhaji and M. Zare, $ZnAl_2O_4$: Ce^{3+} phosphors: study of crystal structure, microstructure, photoluminescence properties and efficient adsorption of Congo red dye, *J. Mol. Struct.*, 2021, **1228**, 129769.

6 G. Ertl, R. Hierl, H. Knözinger, N. Thiele and H. Urbach, XPS study of copper aluminate catalysts, *Appl. Surf. Sci.*, 1980, **5**, 49.

7 K. L. Scrivener, J.-L. Cabiron and R. Letourneux, High-performance concretes from calcium aluminate cements, *Cem. Concr. Res.*, 1999, **29**, 1215.

8 N. Bayal and P. Jeevanandam, Synthesis of metal aluminate nanoparticles by sol–gel method and studies on their reactivity, *J. Alloys Compd.*, 2012, **516**, 27.

9 T. Yamamoto, T. Tanaka, S. Suzuki, R. Kuma, K. Teramura, Y. Kou, T. Funabiki and S. Yoshida, NO reduction with Co in the presence of O_2 over Cu/Al_2O_3 (3)–structural analysis of active species by means of XAFS and UV/Vis/NIR spectroscopy, *Top. Catal.*, 2002, **18**, 113.

10 I. Mindru, D. Gingasu, L. Patron, G. Marinescu, J. M. Calderon-Moreno, S. Preda, O. Oprea and S. Nita, Copper aluminate spinel by soft chemical routes, *Ceram. Int.*, 2016, **42**, 154.

11 E. C. Marques, R. M. Friedman and D. J. Dahm, The structure of copper aluminate: cation distribution at different temperatures and its implications for Cu/Al_2O_3 catalysts, *Appl. Catal.*, 1985, **19**, 387.

12 M. A. Triana, E.-L. Hsiang, C. Zhang, Y. Dong and S.-T. Wu, Luminescent nanomaterials for energy-efficient display and healthcare, *ACS Energy Lett.*, 2022, **7**, 1001.

13 C. Moretti, X. Tao, L. Koehl and V. Koncar, Electrochromic textile displays for personal communication, in *Smart textiles and their applications*, Elsevier, 2016, pp. 539–568.

14 Y. T. Guo and Y. M. Huang, Green aluminate phosphors used for information display, in *Key Engineering Materials*, Trans Tech Publ., 2010, vol. 428, pp. 421–425.

15 K. Yokota, S.-X. Zhang, K. Kimura and A. Sakamoto, Eu^{2+}-activated barium magnesium aluminate phosphor for plasma displays–phase relation and mechanism of thermal degradation, *J. Lumin.*, 2001, **92**, 223.

16 D.-S. Xing, K.-W. Cheah, P.-Y. Cheng, J. Xu, J.-X. Shi, H.-B. Liang and M.-L. Gong, A novel blue magnesium strontium aluminate-based phosphor for PDP application, *Solid State Commun.*, 2005, **134**, 809.

17 C. Ragupathi, J. J. Vijaya, L. J. Kennedy and M. Bououdina, Nanostructured copper aluminate spinels: Synthesis, structural, optical, magnetic, and catalytic properties, *Mater. Sci. Semicond. Process.*, 2014, **24**, 146.

18 V. Kirankumar and S. Sumathi, Structural, optical, magnetic and photocatalytic properties of bismuth doped copper aluminate nanoparticles, *Mater. Chem. Phys.*, 2017, **197**, 17.

19 W. Lv, Z. Luo, H. Yang, B. Liu, W. Weng and J. Liu, Effect of processing conditions on sonochemical synthesis of nanosized copper aluminate powders, *Ultrason. Sonochem.*, 2010, **17**, 344.

20 W. Lv, B. Liu, Q. Qiu, F. Wang, Z. Luo, P. Zhang and S. Wei, Synthesis, characterization and photocatalytic properties of spinel $CuAl_2O_4$ nanoparticles by a sonochemical method, *J. Alloys Compd.*, 2009, **479**, 480.

21 J.-u. Yang, J. H. Cho and M. J. Yoo, Selective metallization on copper aluminate composite *via* laser direct structuring technology, *Composites, Part B*, 2017, **110**, 361.

22 V. Elakkiya, R. Abhishekram and S. Sumathi, Copper doped nickel aluminate: Synthesis, characterisation, optical and colour properties, *Chin. J. Chem. Eng.*, 2019, **27**, 2596.

23 P. Arunkumar, R. Aadhavan, S. Bhanuchandar and K. S. Babu, Effect of fuel ratio on combustion synthesis and properties of magnetic nanostructures, *Mater. Res. Express*, 2014, **1**, 035011.

24 Y. Vidya, K. Anantharaju, H. Nagabhushana, S. Sharma, H. Nagaswarupa, S. Prashantha, C. Shivakumara, *et al.*, Combustion synthesized tetragonal ZrO_2: Eu^{3+} nanophosphors: structural and photoluminescence studies, *Spectrochim. Acta, Part A*, 2015, **135**, 241.

25 I. Gosens, J. A. Post, L. J. de la Fonteyne, E. H. Jansen, J. W. Geus, F. R. Cassee and W. H. de Jong, Impact of agglomeration state of nano-and submicron sized gold particles on pulmonary inflammation, *Part. Fibre Toxicol.*, 2010, **7**, 37.

26 S. Tripathy and D. Bhattacharya, Rapid synthesis and characterization of mesoporous nanocrystalline $MgAl_2O_4$ *via* flash pyrolysis route, *J. Asian Ceram. Soc.*, 2013, **1**, 328.

27 K. Waldner, R. Laine, S. Dhumrongvaraporn, S. Tayaniphan and R. Narayanan, Synthesis of a double alkoxide precursor

to spinel (MgAl$_2$O4) directly from Al(OH)$_3$, MgO, and triethanolamine and its pyrolytic transformation to spinel, *Chem. Mater.*, 1996, **8**, 2850.

28 T. Hinklin and R. Laine, Synthesis of metastable phases in the magnesium spinel- alumina system, *Chem. Mater.*, 2008, **20**, 553.

29 L. Zhong and K. Yun, Graphene oxide-modified zno particles: synthesis, characterization, and antibacterial properties, *Int. J. Nanomed.*, 2015, **10**, 79.

30 P. Chauhan and A. Kumar, Development of a microbial coating for cellulosic surface using aloe vera and silane, *Carbohydr. Polym. Technol. Appl.*, 2020, **1**, 100015.

31 P. Bhavani, A. Manikandan, P. Paulraj, A. Dinesh, M. Durka and S. A. Antony, Okra (abelmoschus esculentus) plant extract-assisted combustion synthesis and characterization studies of spinel ZnAl$_2$O$_4$ nano-catalysts, *J. Nanosci. Nanotechnol.*, 2018, **18**, 4072.